Materials Horizons

ROYAL SOCIETY OF CHEMISTRY

COMMUNICATION

View Article Online
View Journal

Cite this: DOI: 10.1039/d5mh02094h

Received 4th November 2025,
Accepted 12th January 2026

DOI: 10.1039/d5mh02094h

rsc.li/materials-horizons

Orientation-engineered epitaxial $BiVO_4$ thin films for efficient photoelectrochemical glycerol valorization

Minjoo Lee,†[a] Jun Beom Hwang,†[a] Yoonsung Jung,[a] Jiwoong Yang,[a] Yunseo Jang,[a] Inhyeok Oh,[a] Yejoon Kim,[a] Yong-Ryun Jo[b] and Sanghan Lee *[a]

Epitaxial $BiVO_4$ photoanodes with precisely controlled crystallographic orientations were fabricated to elucidate the intrinsic influence of facet anisotropy on photoelectrochemical (PEC) glycerol oxidation. The *b*-axis-oriented (0*k*0) $BiVO_4$ film exhibited a 2.4-fold higher photocurrent density and a 2.6-fold greater charge-separation efficiency than the *c*-axis-oriented (00*l*) film, achieving a production rate of 81.4 mmol m^{-2} h^{-1} under AM 1.5 G illumination. PEC and charge-transfer analyses reveal that the enhanced activity of the (0*k*0) facet originates primarily from improved bulk charge separation and transport rather than surface catalytic effects. This work establishes crystallographic orientation control as an effective design strategy for developing energy-efficient oxide photoanodes for solar-driven glycerol oxidation beyond conventional water splitting.

New concepts

Previous studies on photoelectrochemical glycerol oxidation have predominantly employed polycrystalline or textured $BiVO_4$ films, where the coexistence of multiple orientations and surface terminations obscured the intrinsic role of crystallographic anisotropy. As a result, the fundamental relationship between orientation and glycerol oxidation activity has remained unexplored. In this work, we establish an epitaxial model platform consisting of (00*l*)- and (0*k*0)-oriented $BiVO_4$ thin films grown by pulsed laser deposition, in which orientation is isolated as the only variable under similar structural and chemical environments. This model system allows, for the first time, a direct evaluation of how orientation governs charge separation and oxidation kinetics in the glycerol valorization pathway. The finding that bulk charge-transport anisotropy dictates overall glycerol oxidation reaction performance transforms crystallographic orientation from a structural descriptor into a functional design parameter. This insight establishes crystallographic orientation as an active design parameter for tuning charge transport and oxidation behavior in oxide photoanodes.

Introduction

The rapid increase in global energy consumption has intensified greenhouse gas emissions, underscoring the urgent need for sustainable energy conversion technologies. Among various strategies, hydrogen is regarded as a clean, high-energy-density carrier (142 kJ g^{-1}) with excellent storability and transportability. Solar-driven photoelectrochemical (PEC) water splitting is one of the most promising routes toward green hydrogen production and carbon neutrality. However, the oxygen evolution reaction (OER) at the photoanode suffers from sluggish kinetics and a large overpotential, which fundamentally limits overall PEC efficiency. In addition, oxygen, a product of negligible market value (≈0.11 USD kg^{-1}), further undermines its economic viability.[1] Replacing the OER with a thermodynamically more favorable oxidation that generates value-added chemicals therefore provides dual benefits in both energetic and economic aspects.[2–6]

The PEC glycerol oxidation reaction (GOR) has recently emerged as an attractive alternative anodic reaction.[7–10] Glycerol, an inexpensive by-product of biodiesel production (≈0.75 USD kg^{-1}), contains three hydroxyl groups that enable multistep oxidation to high-value chemicals such as glyceric, glycolic, and formic acids (≈126, 188, 97 USD kg^{-1}, respectively).[9,11,12] The reaction proceeds at a much lower potential (≈0.7–0.9 V *vs.* the reversible hydrogen electrode (RHE, V_{RHE})) than the OER, enabling concurrent hydrogen evolution at reduced bias. Consequently, coupling hydrogen generation with glycerol oxidation enhances both energy efficiency and system profitability. Nevertheless, despite extensive efforts including dopant incorporation, oxygen-vacancy engineering, and heterojunction design, bulk charge recombination and inefficient carrier transport still restrict PEC GOR performance.[13–19]

[a] Department of Materials Science and Engineering, Gwangju Institute of Science and Technology, Gwangju, 61005, Republic of Korea. E-mail: sanghan@gist.ac.kr
[b] GIST Advanced Institute of Instrumental Analysis (GAIA), Electron Microscopy Laboratory, Gwangju Institute of Science and Technology, Gwangju, 61005, Republic of Korea
† These authors contributed equally to this work.

Controlling the crystallographic orientation of oxide semiconductors has proven to be an effective strategy to overcome intrinsic charge-transport bottlenecks.[20] Monoclinic $BiVO_4$ (a = 5.195 Å, b = 5.092 Å, c = 11.701 Å, β = 90.38°) exhibits pronounced anisotropy in electronic structure and carrier mobility: charge transport along the b-axis (010) is more favorable than along the c-axis (001). In our previous work, we fabricated epitaxial $BiVO_4$ thin films with well-defined (001) and (010) orientations, revealing that the b-axis-oriented $BiVO_4$ exhibited superior charge-separation efficiency and photocurrent density during PEC water oxidation.[21] This demonstrates that crystallographic orientation directly governs bulk charge transport and overall PEC performance.[21–23] Building on this, subsequent studies have reported that the exposed facet also affects catalytic behavior.[24–27] For instance, hydrothermally grown or polycrystalline $BiVO_4$ photoanodes with (001)-rich facets have shown faster oxidation kinetics than those dominated by (112) or (101).[10,21,28,29] However, such polycrystalline systems inherently contain mixed grains and heterogeneous interfaces, making it difficult to isolate the intrinsic orientation effect.[24,28,30] Therefore, a comprehensive orientation-resolved investigation using epitaxial $BiVO_4$ for glycerol oxidation remains scarce.

Here, we extend the orientation-controlled epitaxial $BiVO_4$ platform from water oxidation to PEC glycerol valorization. (00l)- and (0k0)-oriented $BiVO_4$ films were grown by pulsed-laser deposition (PLD) to decouple crystallographic anisotropy from other structural variables and directly correlate orientation with GOR activity.[31–34] The (0k0)-oriented $BiVO_4$ film demonstrated substantially enhanced performance compared with the (00l) orientation, showing a 2.6-fold increase in charge-separation efficiency, a 2.4-fold higher photocurrent density, and nearly threefold greater production rate (81.4 *vs.* 25.8 mmol m^{-2} h^{-1}) under AM 1.5 G illumination. These findings provide the first direct evidence that crystal orientation governs GOR activity even in complex organic oxidation, confirming that the anisotropic charge-transport behavior previously observed in water oxidation also dictates multi-electron alcohol conversion reactions. This work establishes an orientation-engineering framework for facet-driven photoanodes, advancing solar-driven glycerol oxidation beyond conventional OER-based PEC systems.

Results and discussion

Epitaxial $BiVO_4$ thin films with distinct crystallographic orientations were fabricated using an *in situ* pulsed laser deposition (PLD) system equipped with a carousel target exchange unit (Fig. 1a).[21,35,36] This configuration enabled precise control of the stacking sequence through target rotation and of the film thickness *via* laser pulse count. The c-axis-oriented $BiVO_4$ (00l) film was grown on YSZ (001) with an indium tin oxide (ITO) conducting buffer layer, whereas the b-axis-oriented $BiVO_4$ (0k0) film was deposited on STO (001) with a $SrRuO_3$ (SRO) buffer layer (yellow and purple schematic boxes in Fig. 1a). The lattice mismatch between $BiVO_4$ and each the respective substrates, calculated as $\text{mismatch}\,(\%) = \frac{a_{\text{film}} - a_{\text{sub}}}{a_{\text{sub}}} \times 100$, was less than 1% for both heterostructures (as indicated in Fig. 1a), ensuring coherent in-plane alignment. In the $BiVO_4$ (00l)/ITO/YSZ, the nearly identical lattice constants enable conventional lattice-matching epitaxy, whereas the $BiVO_4$ (0k0)/SRO/STO combination follows a domain-matching mechanism, where in-plane periodicity is preserved through integer-multiple registry

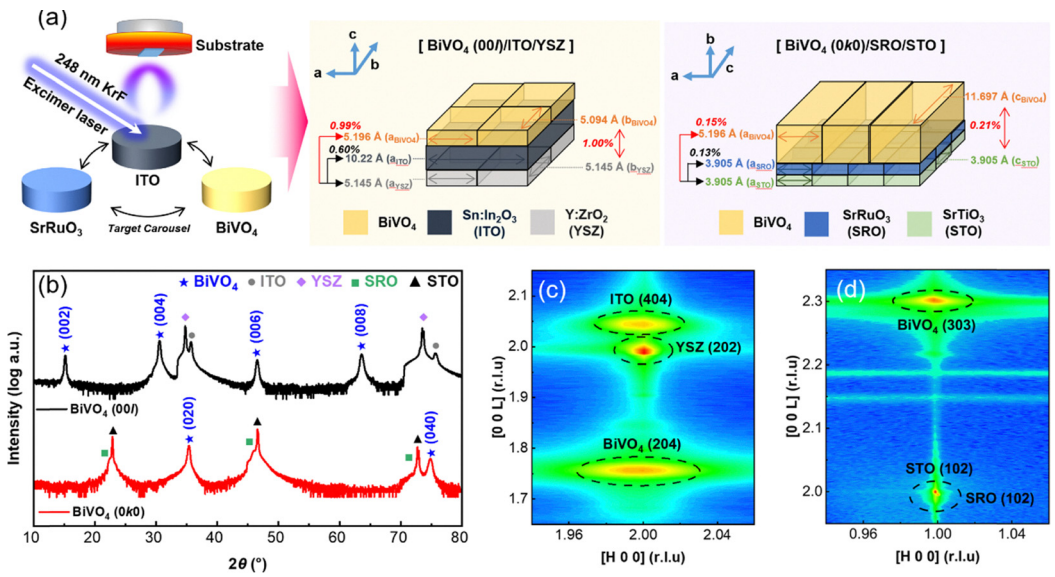

Fig. 1 (a) Schematic illustration of the fabrication process *via in situ* pulsed laser deposition system and the growth of $BiVO_4$ (00l) thin films along the c-axis on YSZ (001) substrates and $BiVO_4$ (0k0) thin films along the b-axis on STO (001) substrates. (b) Out-of-plane X-ray diffraction (XRD) θ–2θ scans of epitaxial $BiVO_4$ thin films with different crystallographic orientations. (c) Reciprocal space map (RSM) of an epitaxial $BiVO_4$ (00l) thin film around the (202) diffraction peak of the YSZ (001) substrate. (d) RSM of an epitaxial $BiVO_4$ (0k0) thin film around the (102) diffraction peak of the STO (001) substrate.

between the $BiVO_4$ and substrate unit cells. Such structural coherence facilitates strain-relaxed epitaxial growth, as schematically illustrated on the right of Fig. 1a.[37] We additionally constructed orientation specific energy level diagrams based on ultraviolet-visible (UV-vis) absorption spectroscopy and ultraviolet photoelectron spectroscopy (UPS) measurements to provide a clearer picture of the band edge positions and carrier extraction through the conducting buffer layers. The resulting band diagrams and schematic energy alignment for the full PEC configuration are provided in Fig. S1 and S2. The out-of-plane X-ray diffraction (XRD) θ–2θ scans (Fig. 1b) clearly demonstrate orientation-specific diffraction features. For $BiVO_4$ (00l)/ITO/YSZ, distinct reflections corresponding to the (002), (004), (006), and (008) planes were observed at 15.18°, 30.55°, 46.53°, and 63.58°, respectively, confirming a pure (00l) orientation without secondary phases. In contrast, $BiVO_4$ (0k0)/SRO/STO exhibited only (020) and (040) reflections at 35.40° and 74.82°, indicating a single (0k0) orientation. Rocking-curve analysis of the (004) and (020) reflections yielded comparable full widths at half maximum (FWHM) of 0.74° and 0.77°, respectively, demonstrating that both films possess similar crystalline quality (Fig. S3). High-resolution reciprocal space mapping (RSM) was employed to determine the in-plane epitaxial relationship of the $BiVO_4$ thin films. As shown in Fig. 1c, the RSM pattern of $BiVO_4$ near the (202) reflection of the YSZ (001) substrate shows a single, well-aligned (204) diffraction spot, confirming in-plane epitaxial registry. Based on the (204) peak position, the lattice parameters of the $BiVO_4$ (00l) film were calculated as 5.163 Å (in-plane) and 11.703 Å (out-of-plane), corresponding to an orientation relationship of $BiVO_4$ (001) ∥YSZ (001). Similarly, for the $BiVO_4$ (0k0) film on STO (001), the RSM pattern (Fig. 1d) shows a single (303) diffraction peak of $BiVO_4$ aligned with the (102) peak of STO. The calculated lattice parameters were 5.216 Å and 11.806 Å (in-plane), confirming the relationship $BiVO_4$ (010)∥STO (001). These results verify that both films were epitaxially aligned in both out-of-plane and in-plane directions. To further elucidate the in-plane epitaxial registry, φ-scans were conducted. For the $BiVO_4$ (00l) film on YSZ (001), both YSZ (204) and $BiVO_4$ (208) reflections exhibited fourfold symmetry with 90° separation, indicative of cube-on-cube epitaxy with 90° twin domains, where $BiVO_4$ [100] is parallel to YSZ [100] or [010] (Fig. S4a). Likewise, for the $BiVO_4$ (0k0) film on STO (001), φ-scans of the STO (103) and $BiVO_4$ (112) reflections displayed fourfold symmetric peaks, demonstrating that $BiVO_4$ [100] is parallel to STO [110] or [1$\bar{1}$0].[38] Together, these analyses confirm coherent in-plane epitaxy with 90° twin relationships, evidencing highly ordered crystalline alignment across the film–substrate interface (Fig. S4b). Overall, these results demonstrate that $BiVO_4$ thin films can be epitaxially grown with two distinct orientations, (00l) and (0k0), while maintaining comparable crystallinity and lattice coherence. Such structural precision provides a robust foundation for systematically investigating the anisotropic charge-transport behavior and facet-dependent photoelectrochemical reactivity of $BiVO_4$ during glycerol oxidation and related solar-driven reactions.[34]

Epitaxial $BiVO_4$ thin films with (00l) and (0k0) orientations were comprehensively characterized to clarify how crystallographic orientation affects their structural and morphological properties. Cross-sectional SEM images (Fig. S5a and b) reveal uniform multilayer architectures, with ∼100 nm $BiVO_4$ layers on ∼50 nm ITO or ∼20 nm SRO bottom electrodes for the (00l) and (0k0) films, respectively. 8°-tilted top SEM images (Fig. S6a and b) further confirms smooth, dense morphology of both films. Consistently, AFM images (Fig. S7a and b) show homogeneous topographies with comparable root-mean-square roughness (R_q) values of 2.44 and 2.29 nm for the (00l) and (0k0) films, respectively (Fig. S7c). The calculated surface areas within the same scan region were ∼9.03 μm^2 for both samples, indicating that surface area does not contribute to any PEC performance differences. XPS spectra (Fig. S8a–c) confirm that both $BiVO_4$ films possess nearly identical Bi 4f, V 2p, and O 1s core-level features, demonstrating consistent stoichiometry irrespective of orientation. Deconvolution of the O 1s region reveals similar contributions from lattice oxygen (O_L) and chemisorbed oxygen species (O_{abs}), suggesting that the overall surface oxygen environment is nearly consistent between the two orientations. Raman spectra (Fig. S9) display the characteristic monoclinic $BiVO_4$ vibrational modes: symmetric and asymmetric bending (δ_s, δ_{as}) of $(VO_4)^{3-}$ at 330–400 cm^{-1}, asymmetric stretching (ν_{as}) at 610 cm^{-1} and 700–750 cm^{-1}, and symmetric stretching (ν_s) at 820–830 cm^{-1}.[39] The nearly identical peak positions and relative intensities indicate that the VO_4 tetrahedral framework remains unaffected by orientation.

Further investigation of the structural properties for epitaxial $BiVO_4$ thin films with different crystallographic orientations was performed by high-resolution transmission electron microscopy (HRTEM) as shown in Fig. 2. HRTEM images for epitaxial $BiVO_4$ thin films with different crystallographic orientations were taken along the $[100]_{substrate}$ zone axis and can identify well-aligned lattice fringes in each layer and at the interfaces between them, suggesting highly single crystalline $BiVO_4$ thin films were grown epitaxially. In the $BiVO_4$ (00l) film on ITO-buffered YSZ (001), the measured spacing of $d_{(002)}$ = 5.87 Å for $BiVO_4$, and $d_{(002)}$ = 5.05 Å for ITO, match theoretical values.[21] Similarly, for the $BiVO_4$ (0k0) film on SRO-buffered STO (001), $d_{(020)}$ = 2.53 Å for $BiVO_4$ and $d_{(001)}$ = 3.88 Å for SRO agree with bulk parameters.[21] FFT patterns (Fig. 2c and d) confirm these epitaxial relationships: $BiVO_4$ (011)/(002) and ITO (020)/(022)/(002) reflections share a [100] zone axis, verifying c-axis-oriented growth, whereas $BiVO_4$ (024)/(004)/(020) and SRO (001)/(011) reflections correspond to b-axis orientation (Fig. 2g and h). SAED patterns (Fig. S10) verify long-range epitaxial order consistent with XRD results, and TEM–EDS elemental mapping (Fig. S11 and S12) reveals atomically sharp interfaces with no interdiffusion. Elemental distributions confirm that Bi, V, In, Sn, Y and Zr are confined within the $BiVO_4$, ITO, and YSZ layers of the (00l) film, while Bi, V, Sr, Ru, and Ti remain localized in the $BiVO_4$, SRO, and STO layers of the (0k0) film. To ensure equivalent electrical conditions for PEC comparison, the resistive properties of the bottom electrodes were evaluated.

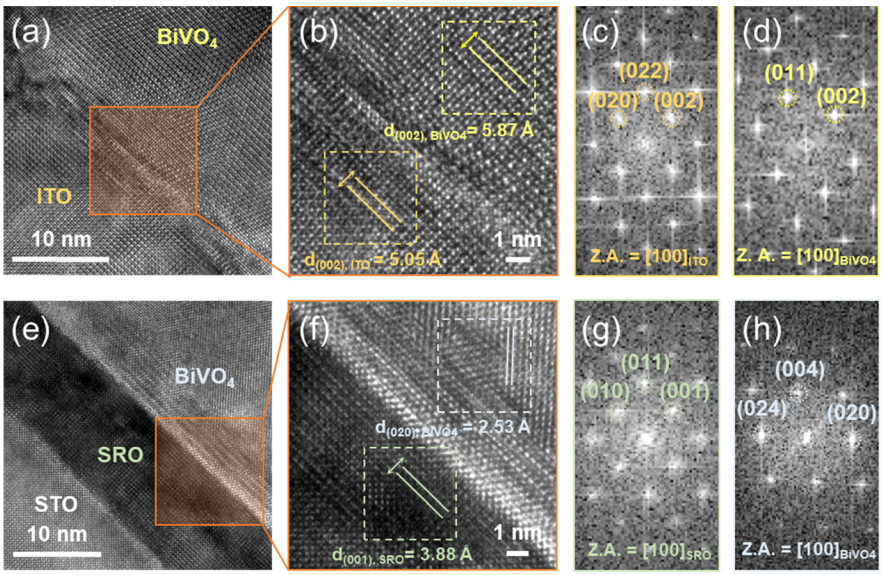

Fig. 2 High-resolution transmission electron microscopy (HRTEM) analysis of epitaxial $BiVO_4$ thin films with different crystallographic orientations. (a) Cross-sectional HRTEM image for an epitaxial $BiVO_4$ film grown on an ITO-buffered YSZ (001) substrate. (b) Enlarged HRTEM image of the boxed region in (a) highlighting the $BiVO_4$/ITO interface. The dashed boxes indicate the areas used for fast Fourier transform (FFT) analysis. The dashed boxes indicate the areas used for fast Fourier transform (FFT) analysis. (c and d) FFT patterns obtained from the ITO and $BiVO_4$ regions in (b), respectively. (e) Cross-sectional HRTEM image of an epitaxial $BiVO_4$ film grown on an SRO-buffered STO (001) substrate. (f) Enlarged HRTEM image of the boxed region in (e) highlighting the $BiVO_4$/SRO interface, with dashed boxes indicating the FFT sampling areas. (g and h) FFT patterns obtained from the SRO and $BiVO_4$ regions in (f), respectively. Lattice fringe spacings were estimated from the marked line profiles in (b) and (f).

The ITO layer exhibited R_s = 88 Ω sq^{-1} and $\rho = 4.4 \times 10^{-4}$ Ω cm, while the SRO layer showed R_s = 131 Ω sq^{-1} and $\rho = 2.6 \times 10^{-4}$ Ω cm (Fig. S13), confirming comparable out-of-plane conductivities in both systems. Collectively, the AFM, XPS, Raman, TEM, SEM, UV-Vis, and electrical analyses confirm that the $BiVO_4$ (00*l*) and (0*k*0) films are equivalent in structural, compositional, and optical aspects, differing only in crystallographic orientation. This structural equivalence provides a robust foundation for evaluating the intrinsic role of orientation in governing PEC performance.

The successful control of exposed facets in $BiVO_4$ photoanodes enabled a systematic investigation into the correlation between PEC GOR activity and crystallographic orientation.[20]

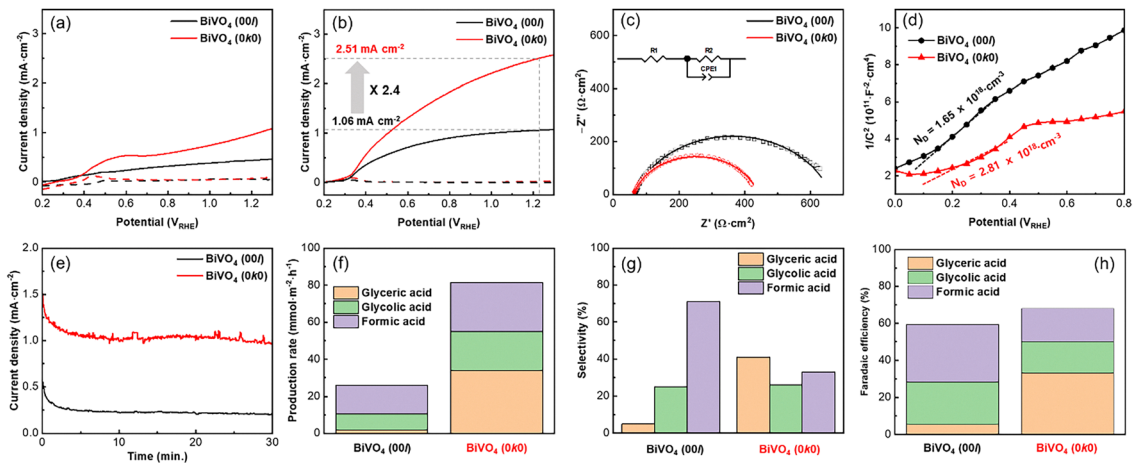

Fig. 3 (a and b) Linear-sweep voltammetry (LSV) curves of $BiVO_4$ (00*l*) and (0*k*0) photoanodes in different electrolytes under 1.5G illumination, with dotted line indicating the corresponding dark currents. (a) 0.1 M KOH, (b) 0.1 M KOH + 1.0 M glycerol. (c) Electrochemical impedance spectroscopy (EIS) Nyquist plots measured at 1.23 V_{RHE} (inset shows the equivalent circuit used for fitting), (d) Mott–Schottky plots of $BiVO_4$ (00*l*) and (0*k*0) photoanodes measured in 0.1 M KOH + 1.0 M glycerol under dark conditions. (e) Chronoamperometry analysis measured at 1.0 V_{RHE} in 0.1 M KOH + 1.0 M glycerol under AM 1.5G illumination, (f) production rates, (g) selectivity, and (h) faradaic efficiency for glyceric acid, glycolic acid, and formic acid quantified by HPLC during PEC glycerol oxidation at 1.0 V_{RHE}.

PEC GOR performance was evaluated in 0.1 M KOH containing 1.0 M glycerol under AM 1.5 G illumination. Under OER conditions (Fig. 3a), the (00*l*)-oriented $BiVO_4$ photoanode showed a photocurrent density of 0.45 mA cm^{-2} at 1.23 V_{RHE}, whereas the (0*k*0)-oriented film exhibited a much higher current density of 1.01 mA cm^{-2}, indicating that the (0*k*0) orientation facilitates more efficient charge transport and surface reaction kinetics. Upon introducing glycerol into the electrolyte (Fig. 3b), both electrodes showed a pronounced enhancement in photocurrent across the entire potential range. The (0*k*0)-$BiVO_4$ achieved 2.51 mA cm^{-2} at 1.23 V_{RHE}—approximately 2.4 times higher than the (00*l*)-oriented film (1.06 mA cm^{-2})—demonstrating the superior photoactivity of the *b*-axis-oriented facet. Additional PEC GOR activity tests in near-neutral and acidic electrolytes are provided in Fig. S14, confirming that the orientation-dependent trend is maintained across different pH environments. Electrochemical impedance spectroscopy (EIS) performed at 1.23 V_{RHE} (Fig. 3c) revealed series resistances (R_s) of 66.6 and 64.1 Ω cm^2, and charge-transfer resistances (R_{ct}) of 633 and 425 Ω cm^2 for the (00*l*)- and (0*k*0)-$BiVO_4$ films, respectively. The markedly lower R_{ct} of the (0*k*0) film highlights its enhanced interfacial charge separation and transfer efficiency. To further probe the orientation dependent electronic properties of the epitaxial $BiVO_4$ films, Mott–Schottky analysis was performed under dark conditions to estimate the donor density and compare the space charge characteristics of the two facets (Fig. 3d). The (0*k*0) oriented $BiVO_4$ film exhibits a noticeably smaller slope than the (00*l*) film, corresponding to a higher donor density. Specifically, the extracted N_D values are 2.81 × 10^{18} cm^{-3} for the (0*k*0) film and 1.65 × 10^{18} cm^{-3} for the (00*l*) film. The higher donor density of the (0*k*0) orientation is consistent with its improved electrical conductivity and more efficient carrier transport, which agrees with the higher photocurrent densities observed under both OER and GOR conditions. Chronoamperometry at 1.0 V_{RHE} under PEC GOR conditions (Fig. 3e) was used to monitor the photocurrent during operation. Quantitative analysis of the oxidation products was carried out by high-performance liquid chromatography (HPLC) to evaluate orientation dependent activity (production rate, selectivity, and faradaic efficiency), as shown in Fig. 3f–h and details are summarized on Table S1. To capture the product dynamics under operation, the liquid products were quantified at different reaction times (Fig. S15). The (0*k*0) $BiVO_4$ sample exhibited a total production rate of 81.4 mmol m^{-2} h^{-1} at 30 min, which was markedly higher than that of the (00*l*) oriented $BiVO_4$ (25.8 mmol m^{-2} h^{-1}). Product distribution analysis further revealed that the (00*l*) film mainly yielded formic acid, whereas the (0*k*0) $BiVO_4$ produced a larger fraction of glyceric acid at the early stage. Notably, the product distribution evolves with reaction time, most clearly on the (0*k*0) film, where the relative contribution of glyceric acid decreases while formic acid becomes more pronounced at longer reaction times, consistent with a consecutive oxidation network under sustained bias. Additional time dependent product analysis performed at a lower bias of 0.8 V_{RHE} shows a comparable evolution trend and is provided in Fig. S16 with quantitative values summarized in Table S2. For independent verification of the HPLC peak assignments, we additionally performed ^{1}H NMR on the post reaction electrolyte collected after 30 min operation at 1.0 V_{RHE} (Fig. S17). This facet dependent trend, together with the enhanced charge utilization efficiency of the (0*k*0) film, suggests that crystallographic orientation influences the overall PEC activity and product distribution. The orientation dependent behavior may originate from intrinsic differences in facet associated carrier

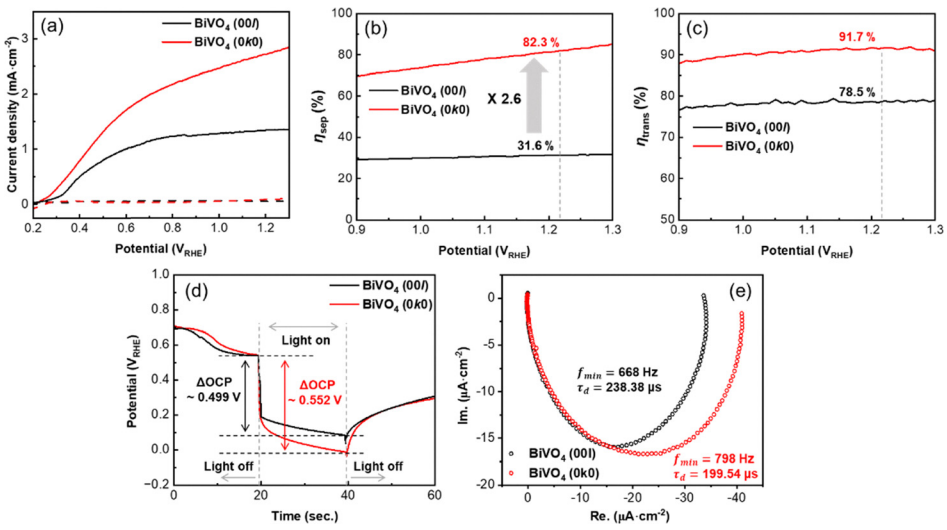

Fig. 4 (a and b) Linear-sweep voltammetry (LSV) curves of $BiVO_4$ (00*l*) and (0*k*0) photoanodes measured in 0.1 M KOH with 1.0 M Na_2SO_3 as a hole scavenger. The dotted lines represent the dark responses. (b) Charge separation efficiency (η_{sep}) and (c) surface charge transfer efficiency (η_{trans}) of $BiVO_4$ (00*l*) and (0*k*0) photoanodes, respectively. (d) Open circuit potential (OCP) transients under chopped illumination for $BiVO_4$ (00*l*) and (0*k*0) photoanodes. (e) Intensity modulated photocurrent spectroscopy (IMPS) complex plane plots for $BiVO_4$ (00*l*) and (0*k*0) photoanodes measured at 1.0 V_{RHE}, with the extracted f_{min} and corresponding electron transport time constant τ_d.

dynamics and surface electronic structure. In particular, Li *et al.* demonstrated that photogenerated electrons and holes are spatially separated on distinct facets of $BiVO_4$, leading to facet dependent redox reactivity.[26] Theoretical analysis has also suggested that low index planes of monoclinic $BiVO_4$ can exhibit different atomic terminations and facet dependent electronic characteristics. Although the direct correlation between facet geometry and the glycerol oxidation pathway remains to be verified, our UPS derived band energetics show only minor differences in work function and band edge positions between the (00*l*) and (0*k*0) films (Fig. S1), suggesting that the distinct PEC GOR behavior is not primarily governed by a large thermodynamic shift in band energetics.

To contextualize the photocurrent changes observed during prolonged PEC GOR operation, we further characterized the films before and after operation using XRD, SEM, AFM, and XPS. These analyses indicate that the epitaxial crystallinity is largely preserved, while surface chemical evolution such as vanadium depletion and changes in the O 1s components is observed after operation, and the detailed results are provided in the SI (Fig. S18–S22 and Tables S3 and S4).

To further clarify the origin of the superior PEC OER and GOR activities of the (0*k*0) $BiVO_4$ photoanode, charge-transfer analyses were conducted (Fig. 4). The LSV curves recorded in the presence of a hole scavenger (0.1 M KOH with 1.0 M Na_2SO_3) showed that the (0*k*0) $BiVO_4$ achieved a much higher photocurrent density nearly twice that of the (00*l*) film at 1.23 V_{RHE}, confirming that the improved PEC performance primarily originates from more efficient bulk charge generation and separation rather than from surface recombination suppression. By comparing the photocurrent responses obtained in the absence (Fig. 3a) and presence of Na_2SO_3, along with UV-vis absorbance spectra (Fig. S1a), the charge-separation (η_{sep}) and charge-transfer efficiency (η_{trans}) were determined (Fig. 4b and c).[37] At 1.23 V_{RHE}, the η_{sep} for the (0*k*0) $BiVO_4$ reached 82.3%, more than twice that of the (00*l*) $BiVO_4$ (31.6%), while η_{trans} values were 91.7% and 78.5%, respectively. Both photoanodes thus exhibit high interfacial charge-transfer capability, but the markedly higher η_{sep} of the (0*k*0) film highlights that its enhanced PEC performance is predominantly governed by improved bulk charge separation and carrier collection. A comparison with representative $BiVO_4$ photoanode studies reported for PEC glycerol oxidation under AM 1.5 G illumination is summarized in Table S5. This comparison highlights that our single crystalline $BiVO_4$ thin films enable, to the best of our knowledge, the first orientation resolved PEC GOR evaluation on single crystalline films and deliver among the highest reported charge separation efficiencies, while maintaining competitive donor density and photocurrent density. Open circuit potential (OCP) transients under chopped illumination were further measured to prove the photovoltage and recombination behavior under zero current condition (Fig. 4d). The photovoltage, evaluated from the OCP difference dark and illuminated states, was larger for the (0*k*0) film, with an absolute OCP shift of 0.552 V compared with 0.499 V for the (00*l*) film. This larger OCP shift indicates a greater quasi Fermi level shifting and more efficient charge separation, which is consistent with the higher η_{sep} observed for the (0*k*0) orientation.[40] In addition, intensity modulated photocurrent spectroscopy (IMPS) was performed to analyze the electron transport kinetics (Fig. 4e). The electron transit time τ_{et} was calculated by: $\tau_d = 1/(2\cdot\pi\cdot f_{min})$, where f_{min} corresponds to the frequency at the minimum imaginary component in the IMPS spectra.[41] The (0*k*0) film exhibited a higher f_{min} of 798 Hz and a shorter τ_d of 199.54 μs than the (00*l*) film with f_{min} of 668 Hz and τ_d of 238.38 μs, indicating faster carrier transport and more efficient charge collection through the film. The shortened transport time reduces the time window for bulk recombination and supports that the facet dependent PEC behavior of $BiVO_4$ is mainly governed by crystallographically controlled bulk charge dynamics that dictate the utilization of photogenerated carriers at the surface.[33,42] Therefore, rational control of crystallographic orientation represents a general design principle for optimizing charge utilization and overall reaction efficiency in oxide-based photoanodes.

Conclusions

In summary, epitaxial $BiVO_4$ thin films with distinct crystallographic orientations were fabricated to elucidate the intrinsic influence of crystal anisotropy on photoelectrocatalytic behavior. Importantly, this work provides the first direct, orientation-resolved demonstration of PEC glycerol oxidation using single-crystalline $BiVO_4$ photoanodes. Structural and electronic analyses confirm that the (00*l*) and (0*k*0) films are identical except for orientation, enabling a direct assessment of orientation-governed charge transport. The *b*-axis-oriented (0*k*0) $BiVO_4$ photoanode shows markedly enhanced performance in both water and glycerol oxidation, with higher photocurrent density, faradaic efficiency, and production of value-added products. Charge-transfer efficiency analysis reveals that this enhancement originates from the intrinsically superior bulk charge-separation capability of the (0*k*0) facet, while both orientations retain comparable surface transfer efficiency. These findings clarify how crystallographic orientation governs anisotropic charge dynamics and establish orientation-controlled epitaxy as an effective route for designing high-efficiency oxide photoanodes for solar-driven glycerol oxidation.

Author contributions

Minjoo Lee: methodology, validation, visualization, investigation, data curation, writing – original draft, formal analysis; Jun Beom Hwang: validation, visualization, investigation, data curation, writing – original draft; Yoonsung Jung: validation, conceptualization; Jiwoong Yang: methodology; Yunseo Jang: formal analysis, data curation, visualization; Inhyeok Oh: formal analysis; Yejoon Kim: data curation, visualization; Yong-Ryun Jo: formal analysis; Sanghan Lee: validation,

investigation, writing – review & editing, supervision, project administration, funding acquisition, conceptualization.

Conflicts of interest

There are no conflicts to declare.

Data availability

Data supporting the findings of this study are available within the main manuscript and the supplementary information (SI). Supplementary information: detailed descriptions of the experimental procedures, characterization methods, and additional supporting data. See DOI: https://doi.org/10.1039/d5mh02094h.

Further relevant data are available from the corresponding author upon reasonable request.

Acknowledgements

This research was supported by the program of Future Hydrogen Original Technology Development (RS-2021-NR057808), through the National Research Foundation of Korea (NRF), funded by the Korean government (Ministry of Science and ICT (MSIT)). This work was supported by the National Research Foundation of Korea (NRF) grant funded by the Korea government (MSIT) (RS-2025-00563779).

References

1 Z. Ke, N. Williams, X. Yan, S. Younan, D. He, X. Song, X. Pan, X. Xiao and J. Gu, *J. Mater. Chem. A*, 2021, **9**, 19975–19983.
2 P. Lianos, *J. Hazard. Mater.*, 2011, **185**, 575–590.
3 P. Panagiotopoulou, M. Antoniadou, D. I. Kondarides and P. Lianos, *Appl. Catal., B*, 2010, **100**, 124–132.
4 B. Seger, G. Q. M. Lu and L. Wang, *J. Mater. Chem.*, 2012, **22**, 10709–10715.
5 M. Antoniadou, P. Bouras, N. Strataki and P. Lianos, *Int. J. Hydrogen Energy*, 2008, **33**, 5045–5051.
6 S. Xie, T. Zhai, W. Li, M. Yu, C. Liang, J. Gan, X. Lu and Y. Tong, *Green Chem.*, 2013, **15**, 2434–2440.
7 Z. Wu, H. Guo, K. Ren, Y. Wang, H. Zhang, F. Zhang, L. Liu, G. Li and L. Qi, *Adv. Mater.*, 2025, e16504.
8 S. H. Roh, Y. Li, J. Y. Kim, W. T. Hong, H. Han, C.-W. Jung, Y. M. Choi, G. M. Noh, Y. S. Jang and K. H. Kim, *Appl. Catal., B*, 2025, 125600.
9 Z. Xie, X. Liu, P. Jia, Y. Zou and J. Jiang, *Energy Adv.*, 2023, **2**, 1366–1374.
10 T.-G. Vo, C.-C. Kao, J.-L. Kuo, C.-C. Chiu and C.-Y. Chiang, *Appl. Catal., B*, 2020, **278**, 119303.
11 J.-A. Lin, I. Roh and P. Yang, *J. Am. Chem. Soc.*, 2023, **145**, 12987–12991.
12 B. Katryniok, H. Kimura, E. Skrzyńska, J.-S. Girardon, P. Fongarland, M. Capron, R. Ducoulombier, N. Mimura, S. Paul and F. Dumeignil, *Green Chem.*, 2011, **13**, 1960–1979.
13 Y. Jung, S. Kim, S. Kim, Y. Kim, J. B. Hwang, D. Y. Kim and S. Lee, *Small*, 2025, **21**, 2409082.
14 L. Wang, Z. Chen, Q. Zhao, N. Wen, S. Liang, X. Jiao, Y. Xia and D. Chen, *Adv. Funct. Mater.*, 2024, **34**, 2409349.
15 H. Sun, R. Tang, L. Wang, Y. Liang, W. Yang, Z. Lin, X. Zhang, K. Chen, W. Liang and S. Zhao, *EES Catal.*, 2025, **3**, 337–346.
16 Y. Liu, H. Shang, B. Zhang, D. Yan and X. Xiang, *ACS Appl. Mater. Interfaces*, 2025, **35**(11), 2417011.
17 S. Kim, Y. Jung, S. So, Y. Kim, S. Seo, J.-C. Park, D.-Y. Kim, J.-H. Lee and S. Lee, *Int. J. Hydrogen Energy*, 2025, **127**, 384–393.
18 Y. Lee, S. Kim, S. Y. Jeong, S. Seo, C. Kim, H. Yoon, H. W. Jang and S. Lee, *Catal. Today*, 2021, **359**, 43–49.
19 S. Kim, E. An, I. Oh, J. B. Hwang, S. Seo, Y. Jung, J.-C. Park, H. Choi, C. H. Choi and S. Lee, *Catal. Sci. Technol.*, 2022, **12**, 5517–5523.
20 Y. Wang, J. Chen, T. Guo, C. Liu, Y. Ma, L. Shi, Z. Tian, Z. H. Alhubail, F. Ming and X. Zhang, *Adv. Mater.*, 2025, e08546.
21 J. Song, M. J. Seo, T. H. Lee, Y.-R. Jo, J. Lee, T. L. Kim, S.-Y. Kim, S.-M. Kim, S. Y. Jeong and S. Lee, *ACS Catal.*, 2018, **8**, 5952–5962.
22 Y. Shi, L. Peng, Y. Ding, Y. Zhao and G. Yu, *Chem. Soc. Rev.*, 2015, **44**, 6684–6696.
23 X. Fang, J. Y. Choi, M. Stodolka, H. T. Pham and J. Park, *Acc. Chem. Res.*, 2024, **57**, 2316–2325.
24 Z. Wu, K. Ren, J. Zhou, Y. Zhang and L. Qi, *Adv. Funct. Mater.*, 2025, **35**, 2418294.
25 W. He, W. Li, J. Liu, G. Lou, C. Zhang, Y. Liu and J. Li, *J. Mater. Chem. A*, 2025, **13**, 7284–7294.
26 M. Yang, Z. Fan, J. Du, R. Li, D. Liu, B. Zhang, K. Feng, C. Feng and Y. Li, *ACS Catal.*, 2022, **12**, 8175–8184.
27 S. Zhang, M. Long, P. Zhang, J. Wang, H. Lu, H. Xie, A. Tang and H. Yang, *Chem. Eng. J.*, 2022, **429**, 132091.
28 T. He, Y. Zhao, D. Benetti, B. Moss, L. Tian, S. Selim, R. Li, F. Fan, Q. Li and X. Wang, *J. Am. Chem. Soc.*, 2024, **146**, 27080–27089.
29 R. Li, F. Zhang, D. Wang, J. Yang, M. Li, J. Zhu, X. Zhou, H. Han and C. Li, *Nat. Commun.*, 2013, **4**, 1432.
30 C. Liu, L. Chen, X. Su, S. Chen, J. Zhang, H. Yang and Y. Pei, *ACS Appl. Mater. Interfaces*, 2021, **14**, 2316–2325.
31 G.-Z. Tu, J.-Y. Chen, Z.-X. Zhen, Y. Li, C.-W. Chang, W.-J. Chang, H. M. Chen and C.-M. Jiang, *ACS Appl. Electron. Mater.*, 2024, **6**, 1872–1885.
32 L.-L. Zheng, L. Tian, D. Wang, Y. Chen, Q.-Q. Tang, Q.-J. Xing, X.-Z. Liu, D.-S. Wu and J.-P. Zou, *Chem. Eng. J.*, 2023, **473**, 145507.
33 B. Zhang, Y. Xiang, M. Guo, J. Wang, K. Liu, W. Lin and G. Ma, *ACS Appl. Energy Mater.*, 2021, **4**, 4259–4268.
34 D. Li, Y. Liu, W. Shi, C. Shao, S. Wang, C. Ding, T. Liu, F. Fan, J. Shi and C. Li, *ACS Energy Lett.*, 2019, **4**, 825–831.

35 J. B. Hwang, J. Lee, G. D. Nam, S. Choi, J. Yang, Y. Jung, Y. Kim, I. Oh, J. H. Joo and S. Lee, *J. Mater. Chem. A*, 2024, **12**, 33789–33798.
36 H. Jang, Y. Kim, H. Choi, J. Yang, Y. Jung, S. Choi, D. Lee, H. W. Jang and S. Lee, *J. Energy Chem.*, 2024, **89**, 71–78.
37 T. W. Kim and K.-S. Choi, *Science*, 2014, **343**, 990–994.
38 V. F. Kunzelmann, C.-M. Jiang, I. Ihrke, E. Sirotti, T. Rieth, A. Henning, J. Eichhorn and I. D. Sharp, *J. Mater. Chem. A*, 2022, **10**, 12026–12034.
39 S. Li, Y. Cheng, Q. Wang, C. Liu and L. Xu, *Mater. Res. Express*, 2020, **7**, 115005.
40 M. Zhong, T. Hisatomi, Y. Kuang, J. Zhao, M. Liu, A. Iwase, Q. Jia, H. Nishiyama, T. Minegishi and M. Nakabayashi, *J. Am. Chem. Soc.*, 2015, **137**, 5053–5060.
41 G. Franco, J. Gehring, L. Peter, E. Ponomarev and I. Uhlendorf, *J. Phys. Chem. B*, 1999, **103**, 692–698.
42 F. Li, H. Yang, Q. Zhuo, D. Zhou, X. Wu, P. Zhang, Z. Yao and L. Sun, *Angew. Chem.*, 2021, **133**, 2004–2013.

